Deuteron NMR Study of Polyaniline and Polyaniline/Clay Nanocomposite

Yanina A. Goddard,[†] Robert L. Vold,*[,†] and Gina L. Hoatson[‡]

Departments of Applied Science and Physics, College of William & Mary, PO Box 8795, Williamsburg, Virginia 23187-8795

Received October 8, 2002

ABSTRACT: Different forms of solid polyaniline (Pani) and polyaniline intercalated into montmorillonite clay layers have been characterized by solid-state deuteron quadrupole echo and magic angle spinning NMR experiments. Quadrupole echo spectra reveal different fractions of fast flipping phenyl rings for conductive emeraldine salt and nonconductive emeraldine base samples. Deuteron MAS spectra of emeraldine salt show two partially resolved sets of sidebands, whose centers are separated by 6.0 ± 1.5 ppm. For conductive polyaniline, the temperature dependence of line widths and intensities is consistent with the existence of metallic domains embedded in a disordered insulating matrix, such that approximately 40% (T = 223 K) to 60% (T = 373 K) of the aromatic deuterons experience a Knight shift. This implies that polarons play an important role in the conductivity mechanism.

I. Introduction

The prospect of combining the conductivity of metals with lightweight and desirable mechanical and optical properties of polymers has attracted much attention to organic, conducting polymers. Among these, polyaniline (Pani) is one of the most technologically important. It is used in batteries,[1−3] in electrochromic devices,[1−4] in gas sensors,[2,4−6] as a corrosion inhibitor,[2,4] as an antistatic agent,[1,3] for shielding against electromagnetic fields,[3,4] in light-emitting devices,[3,4,6,7] for membrane-based separation of gases,[1,3] in electrochemical actuators for "artificial muscle",[3,8] and for preparation of printed circuit boards.[4,6] Pani is unique among conducting polymers because of its relatively high conductivity (∼10^3 S/cm) and air stability.

Pani is usually prepared by chemical or electrochemical oxidation of aniline.[9,10] It can exist in several oxidation states ranging from the completely reduced "leucoemeraldine" base state to the completely oxidized "pernigraniline" state. The most extensively studied form of the polymer is emeraldine, in which the numbers of reduced and oxidized units are equal. A schematic representation of the idealized repeat unit of emeraldine base (EB) is shown in Figure 1A.

EB is an insulator but can be converted to a conducting form by proton doping. Idealized structures of the protonated form, called emeraldine salt (ES), are shown in Figure 1B,C. It has been reported[11] that the predicted room temperature intrinsic conductivity of ES is 10^6 S/cm, which is approximately equal to that of copper. Despite extensive study, basic questions concerning the electronic structure and conductivity of this polymer remain unanswered. These include the nature of the charge carriers (whether polarons, Figure 1B, or spinless bipolarons, Figure 1C), the dimensionality of electrical conduction, and what defects are responsible for failure to observe the high predicted intrinsic conductivity.

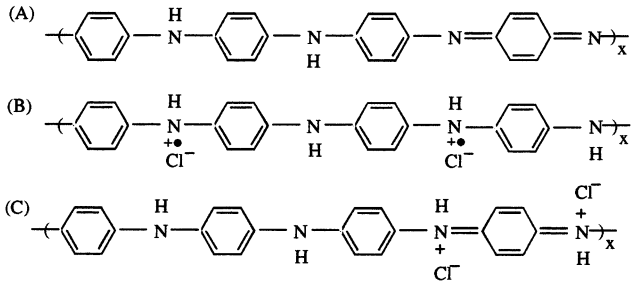

Figure 1. Schematic illustration of ideal repeat unit for (A) emeraldine base, (B) polaron form of emeraldine salt, and (C) bipolaron form of emeraldine salt.

Conducting polymers encapsulated in two-dimensional layers of inorganic ceramics or one-dimensional channels of organic hosts offer fascinating new perspectives. The constrained environment of an inorganic host should lead to a high degree of polymer order within the host, and this may have profound effects on polymer structure, properties, and electrical conduction mechanisms. These systems represent a new class of molecular composites with diverse electrical, optical, mechanical, and thermal properties. Clays are interesting host materials because of their ready availability, small particle size, and well-known propensity for intercalation. Montmorillonite (MMT) is one of the most abundant naturally occurring clay minerals.[12] Its lattice consists of a sheet of octahedral alumina sandwiched between two tetrahedrally coordinated silica sheets. Substituting ions of lower charge for higher charge in both the octahedral (e.g., Mg^{2+} replacing Al^{3+}) and tetrahedral (e.g., Al^{3+} replacing Si^{4+}) sheets produces negatively charged layers. These can expand to accommodate loosely bound hydrated cations, water, and polar organic solvents.[12]

Polyaniline has been extensively studied using ^{13}C,[13,14] ^{15}N,[15] ^{1}H,[16] and ^{2}H[13] NMR. Here we report deuteron NMR studies of emeraldine base, emeraldine salt, and a polyaniline/MMT nanocomposite. Quadrupole echo (QE) line shapes were used to quantify the temperature-dependent fraction of rapidly flipping aromatic rings in the three materials. Deuteron magic angle spinning

[†] Department of Applied Science.
[‡] Department of Physics.
* To whom correspondence should be addressed. E-mail rlv@nmr.physics.wm.edu.

10.1021/ma021563t CCC: $25.00
Published on Web 01/30/2003

(MAS) experiments provided significantly better resolution and improved sensitivity. Unlike emeraldine base, MAS spectra of ring-deuterated emeraldine salt show two partially resolved sideband manifolds, with different line widths and integrated intensities. We believe this is the first observation of a Knight shift in bulk polyaniline.

II. Experimental Procedures and Data Analysis

Material Preparation. Starting materials for polymer synthesis were obtained from Aldrich Chemical Co. and used as received, except for aniline, which was distilled from zinc dust. Emeraldine salt was prepared by oxidizing aqueous HCl solutions of aniline ($C_6H_5NH_2$ or 99 atom % D $C_6D_5NH_2$) with ammonium peroxydisulfate ($(NH_4)_2S_2O_8$) in air at ~3 °C. The precipitate was washed with deionized water and dried under vacuum. Emeraldine hydrochloride was converted to the base by stirring with 0.1 M aqueous solution of ammonium hydroxide (NH_4OH) in air and drying under vacuum.

Sodium montmorillonite was purchased from Southern Clay Products, Inc. The Pani/clay nanocompound was prepared as follows: 4 g of Na−MMT was added to 200 mL of deionized water and stirred for 3.5 h at 70 °C. Then, 0.82 mL of aniline and 1.4 mL of concentrated HCl were added. After stirring for 17 h at 70 °C, the mixture was washed with room temperature deionized water three times. More HCl was added to return the pH to 2, and the mixture was stirred for another hour. 2.023 g of ammonium peroxydisulfate (0.0088 mol) was added. Polymerization lasted for approximately 15 h. The precipitate was isolated by filtration, washed three times with deionized water, and dried under vacuum at ambient temperature.

Material Characterization. The Pani/clay sample was analyzed by X-ray diffraction and Fourier transform infrared spectroscopy. XRD measurements were carried out using a Scientag X1 diffractometer operating at 45 keV and 35 mA with a Ni filter and a Cu source (λ = 15.4 nm). Pure clay showed a broad peak at $2\theta = 9°$, corresponding to interlayer spacing of 7.8 Å, which increased to 13.06 Å upon intercalation of aniline. This suggests that aniline rings are oriented approximately perpendicular to the clay layers. After polymerization, the spacing was slightly smaller, 12.66 Å, in agreement with the suggestion of single layer intercalation and extended chain conformation.[17] XRD spectra of emeraldine base and salt are similar to those reported earlier.[18] A broad, featureless pattern was found for EB; this is characteristic of amorphous polymers. The ES sample exhibited well-defined peaks at $2\theta = 9°$, 15°, 20°, 26°, 28°, and 31°, superimposed on a broad amorphous background. The fraction of crystallinity, determined by estimating the integrated intensity of the peaks above the amorphous background, is approximately 20 ± 5%.

FTIR spectroscopy was performed on pressed disks of Pani/clay dispersed in KBr. The spectra are consistent with the results reported by Wu et al.[17] and exhibit characteristic absorption lines for emeraldine (1563 and 1489 cm^{-1}) and clay (917 and 840 cm^{-1}).

Ambient temperature four-probe dc resistivities of protonated polyaniline salt, base, and clay nanocomposite were measured using MMR Technologies' computer-controlled low-temperature Hall system. Pellets were pressed from powder, using a press with hydraulic pressure of 1700 pounds. Electrical contacts were made with conductive silver epoxy (EPOTEK). Linearity checks were performed to ensure Ohmic contact. Conductivities of salt, base, and Pani/clay are 0.15, 1 × 10^{-9}, and 1 × 10^{-4} S/cm, respectively.

NMR Experiments. Quadrupole echo NMR spectra were recorded using a home-built spectrometer based on a 7 T superconducting magnet, with a 5 mm broad-band, single resonance probe tuned to 46.06 MHz. The quality factor of the probe is Q = 105, determined by matching a line shape simulation to a QE experiment on deuterated polyethylene. The temperature in all NMR experiments was controlled to 0.2 °C by a LakeShore temperature controller (model DRC91-CA), with a 10 kΩ platinum sensing resistor placed close to the sample coil. For emeraldine salt and base, the standard quadrupole echo pulse sequence was used QE: $90x-t-90y-\tau-$ACQ−RD. The 90° pulse length was 1.6 μs, resulting in adequate coverage of the ±250 kHz spectral width. A recycle delay (RD) of 12 s was used for emeraldine base while 10 s was adequate for the salt sample. Partial suppression of slowly relaxing line shape components was achieved with 10 saturation 90° pulses, separated by 1 ms, preceding the QE sequence: $(1m-t-90x)_{10}-$QE (RD = 0.6 s). Since the clay sample has paramagnetic impurities, two 180° refocusing pulses were interleaved in the QE sequence to refocus paramagnetic shifts:[19] $90x-t-180y-t-90y-t-180y-\tau-$ACQ−RD. Recycle delay 0.1 s was adequate for the Pani/clay sample. Data manipulations were performed on O2 Silicon Graphics workstations with locally written routines. An exponential apodization corresponding to 500 Hz Lorentzian broadening was applied to the time domain signal. The data then were left shifted, by spline interpolated fractions of a dwell time if necessary, so that a point occurred precisely at the top of the echo. A zero-order phase correction was used to minimize signal in the out-of phase channel. The small residual asymmetry in the Fourier transform spectra probably arises from instrumental artifacts not fully eliminated by phase cycling. Line shapes were simulated using the EXPRESS simulation package,[20] which is based on numerical solution of the stochastic Liouville equation for jumps among user-defined orientational sites.

Magic angle spinning (MAS) spectra were obtained at 46.06 MHz using Apollo rf components (Tecmag) and a Chemagnetics triple resonance probe with a 5 mm coil, tuned in single channel mode. The quality factor of this probe is Q = 220. One-pulse experiments (90° pulse width was 3.2 μs) were performed with a spectral width of ±200 kHz. The spinning rate was 8000 ± 1 Hz for emeraldine base and salt samples and 7500 ± 3 Hz for the Pani/clay sample. For temperature-dependent measurements the spinning samples were thermally equilibrated for 20 min before data acquisition. At low temperatures, the number of scans was limited by heat conduction to the magnet (typically, less than 2 h for an experiment including thermal equilibration). The free induction decay was Fourier transformed starting at the top of the first rotational echo.

III. Results and Discussion

QE Experiments for Emeraldine Base and Salt. Powder samples of ring deuterated emeraldine base and emeraldine hydrochloride have similar quadrupole echo spectra. In polymers containing backbone phenyl rings 180° ring flips are common and reflect local variations in free volume.[21,22] In Pani, ring flip rates are also influenced by electrostatic interactions with counterions and partial double bond character of the C−N bonds in the quinoid moieties.[13]

Experimental quadrupole echo (A) and presaturation (B) line shapes of ring deuterated emeraldine base at ambient temperature are shown in Figure 2 (solid line). The dashed lines are simulated spectra, calculated using EXPRESS.[20] A simple two-site model was used to simulate the fast flipping component. Presumably, a more accurate representation could be obtained by including distributions of jump angles and rates.[21] For the "rigid" component, a model of jumps among four unequally populated sites (p_0, p_1, p_2, p_3), defining an asymmetric cone, was used, with jump rates ~10^5 s^{-1}. (Other relevant parameters are given in the figure caption.) This "asymmetric libration" model was necessary to reproduce the reduced intensity in the middle of the powder pattern relative to the horns. The input value of quadrupole coupling constant (QCC), 180 kHz, was reduced by the simulation algorithm to match the experimentally observed value, which was, for example, $\langle QCC \rangle$ = 171 ± 1 kHz for EB at ambient temperature. This corresponds to a cone angle 15 ± 2°.

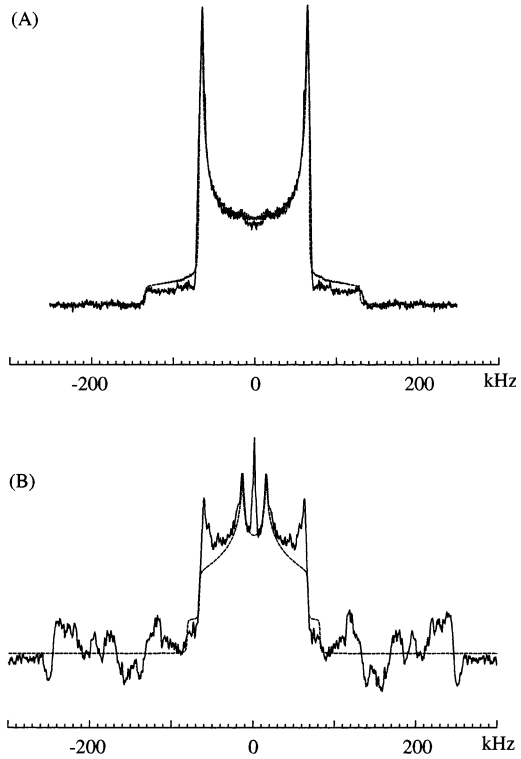

Figure 2. Experimental (solid line) quadrupole echo (A) and presaturation (B) spectra of ring deuterated emeraldine base at ambient temperature compared to EXPRESS simulations (dashed lines). Best fit was achieved with the following parameters: QCC = 180 kHz, $\eta = 0.029$, $k_{lib} = 2.5 \times 10^5\ s^{-1}$, $k_{flip} = 2.5 \times 10^7\ s^{-1}$, cone angle = 15 ± 2°, $p_0 = 0.82$, $p_1 = p_2 = p_3 = 0.06$, with 3% fast flippers.

The QE line shape is a superposition of spectra of fast flipping and rigid rings, as seen in Figure 2. However, as pointed out by Kaplan et al.,[13] this apparent bimodal distribution of flip rates is probably an artifact of the QE experiment, arising from its selective suppression of rapidly dephasing spins with intermediate jump rates. The dynamic heterogeneity is usually interpreted as a manifestation of differences in packing densities.[21] Our experimental results agree qualitatively with data reported by Kaplan et al.[13]

The relative amount of the fast flipping component increases as temperature increases. Presumably, as temperature rises, the free volume increases and rings are less constrained by neighboring chains. At all temperatures EB has a higher fraction of fast flippers than ES. This is attributed to interaction with chloride counterions and/or partial π-electron delocalization in ES. The fractions noted in the figure caption represent the relative (integrated) intensities of the simulated line shapes for slow and fast flippers, which best reproduce the observed equilibrium QE spectrum.

QE Experiment for Pani/Clay. A quadrupole echo spectrum of the Pani intercalated into MMT clay is shown in Figure 3. The narrow feature in the middle of the spectrum is probably due to a small amount of relatively mobile, unreacted aniline$^+$-d_5 trapped in the clay during polymerization. Simulations of the rigid lattice powder pattern show that its mean quadrupole coupling constant QCC = 208 kHz, 15% larger than observed for ES and EB. This is also significantly larger than values reported for highly rigid crystalline materials[23] and probably reflects intermolecular contributions to the deuteron electric field gradient (EFG) arising from

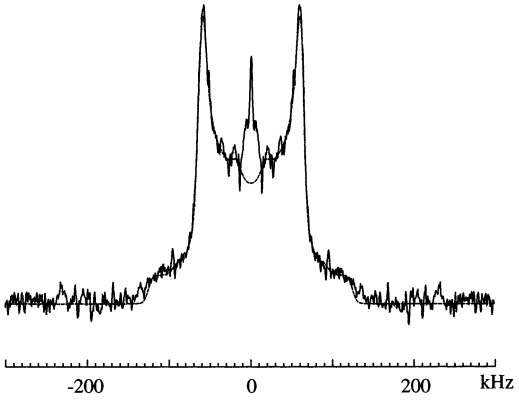

Figure 3. Experimental (solid line) and simulated (dashed line) quadrupole echo spectra of Pani/clay nanocompound at ambient temperature. Best fit parameters are QCC = 208 kHz, $\eta = 0.033$, $k_{lib} = 1 \times 10^7\ s^{-1}$, $k_{flip} = 1.5 \times 10^7\ s^{-1}$, cone angle = 20 ± 4.7°, $p_0 = 0.01$, $p_1 = p_2 = p_3 = 0.33$, with 15% fast flippers.

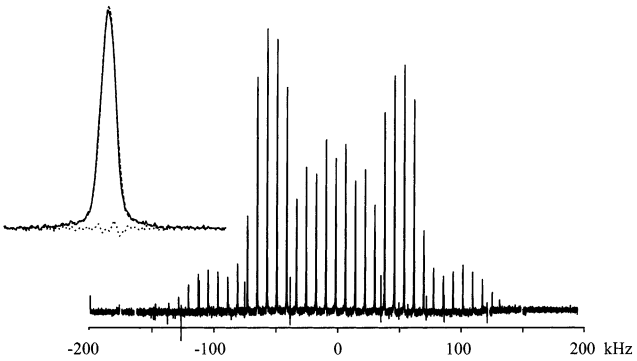

Figure 4. Experimental deuteron MAS spectrum of emeraldine base at 263 K. Spinning speed was 8 kHz. The inset illustrates a spinning sideband. The dashed line is the best fit, achieved by nonlinear Levenburg−Marquardt iterations on a normalized, weighted sum of two Gaussians. The dotted line is the difference between the experimental and calculated data.

nearby charges in the clay layers. These depend inversely on the cube of the distance from the deuteron to the center of charge, and the unusually large Gaussian broadening (9.6 kHz) needed to fit the line shapes is consistent with a dispersion of relevant distances and hence EFG and QCC values.

For the Pani/clay sample the signal-to-noise ratio is not high enough to permit detection of a small fraction of fast flipping aromatic rings, and attempts to selectively saturate the wide powder pattern failed completely due to its short relaxation times ($T_{1Z} \sim 6$ ms). The short relaxation times are an unfortunate consequence of the fact that montmorillonite clay has ~3 wt % iron incorporated as defects in the silica layers.

An intriguing alternative explanation for both the broad QCC distribution and the short relaxation times is that Pani is incorporated in the clay in its electrically conducting salt form. Formation of polarons (Figure 1B) could increase the average value of electric field gradients and the distribution width, and fast relaxation could arise from a Korringa-like mechanism

MAS Experiments. a. Emeraldine Base. The MAS spectrum of EB at 263 K is shown in Figure 4. One spinning sideband is expanded in the inset; the others have similar shapes. The dashed line in the inset represents the best fit of the sideband achieved by nonlinear Levenburg−Marquardt least-squares fitting.

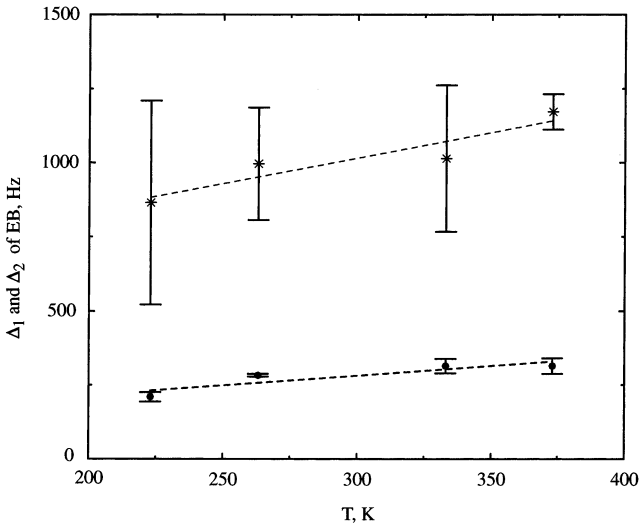

Figure 5. Temperature dependence of the full width at half-heights of narrow Δ_1 (circles) and wide Δ_2 (stars) Gaussian components of emeraldine base. (Dashed lines are drawn to guide the eye.)

A weighted sum of two Gaussians was chosen as the best model function. Details of simulations and analysis of the goodness of fit of the model function are summarized in Appendix A.

To exclude possible influence of the "fast flippers" on data analysis, only sidebands at frequencies of absolute value of 48 kHz and higher were considered. The center frequencies of the two Gaussians (ν_1 and ν_2) of the EB sample are the same within experimental error (±22 Hz) and do not depend on temperature. The relative integrated intensity of the wide peak is 0.22 ± 0.06 and also temperature independent. In principle, this intensity might be underestimated due to more rapid, irreversible dephasing of the wide component at the time of the first rotational echo $\tau_R = 125$ μs. However, the sideband intensities were found to decay as single exponential with the time constant T_2, which decreases from 2.00 ± 0.004 to 0.95 ± 0.02 ms as temperature increases from 223 to 373 K.

The temperature dependence of the full widths at half-height (Δ) of both peaks is shown in Figure 5. Libration of C−D bonds over a range of angles results in an inhomogeneous spread of (quadrupolar) site frequencies, $\delta\omega_q$. If the libration rates are larger than the distribution width, $k \gg \delta\omega_q$, the MAS sideband line width should be proportional to $(\delta\omega_q)^2/k$. Thus, for both broad and narrow components of the EB spectra, the observed increase in MAS line width can be ascribed to increasing librational amplitude (i.e., larger $\delta\omega_q$) which more than compensates for the expected[24] linear temperature dependence of k. Alternatively, the MAS line width could be due to slow libration, in which case the line width is simply proportional to k. Discriminating between these two alternatives (slow libration vs fast) would require adopting untestable functional relations between the libration rate and amplitude. Because of low intensity of the wide Gaussian and consequently large uncertainties, a more detailed analysis of its line width is not warranted.

In the MAS spectra of emeraldine base, the observation of two component sidebands with the same frequency but different widths can be attributed to different librational rates and/or amplitudes of benzoid and quinoid rings. Since the relative intensities of the peaks do not change with temperature and the intensity ratio of narrow to wide peak is approximately equal to the ratio of amine to imine nitrogens (see Figure 1), one can ascribe the wide Gaussian to rigid quinoid rings, which are expected to have smaller libration amplitudes.

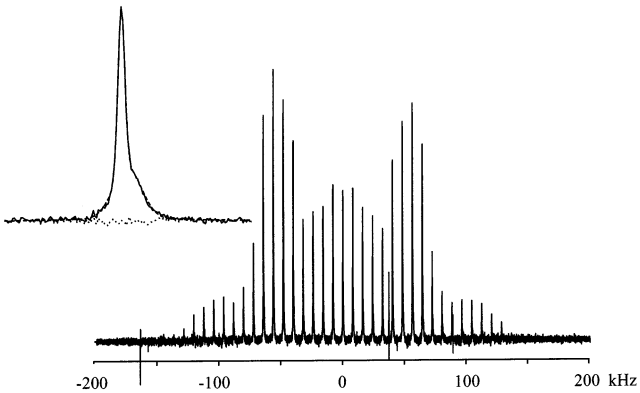

Figure 6. Experimental deuteron MAS spectrum of emeraldine salt at 263 K, spinning at 8 kHz. The inset illustrates an individual spinning sideband. The dashed line is the best fit, achieved by nonlinear Levenburg−Marquardt iterations on a normalized, weighted sum of three Gaussian functions. The dotted line is the difference between the experimental and calculated data.

b. Emeraldine Salt. The MAS spectrum of ES at 263 K is shown in Figure 6. Individual sidebands of the conductive polymer (inset) have two Gaussian peaks, which are at the same frequency as those of EB. In addition, they have a distinctive feature: a partially resolved third Gaussian peak whose center frequency is shifted 6.0 ± 1.5 ppm (for simulation details see Table 3, Appendix A). Table 1 lists the temperature dependence of the fit parameters for the ES sample.

The shift of the third Gaussian is positive and independent of temperature within experimental error, as demonstrated in Figure 7. The magnitude and direction of the shift are consistent with a small hyperfine interaction between aromatic deuterons and electron spins (Knight shift). However, interpretation of this observation as a Knight shift is controversial. In principle, nuclear spins which experience a true Knight shift must also exhibit Korringa-like relaxation behavior.[14,25] For deuterons in ES, the situation is complicated by spectral overlap of powder patterns from conductive and nonconductive regions. Spin diffusion and cross relaxation between spins in different regions leads to complex, nonexponential recovery curves. In highly conducting PANI−CSA films, Kolbert et al.[14] found a constant value $T_1T \sim 100$ s K over a 200 deg temperature range for ^{13}C. Using relevant parameters estimated by Kolbert et al.[14] and correcting for the lower gyromagnetic ratio of deuterons, the 10−15 ppm ^{13}C Knight shift in the conducting film would be consistent with a Korringa-like contribution to ^{2}H relaxation in our sample with $T_1 = 2.5-6$ s at 300 K. We observe shorter relaxation times, $T_1 = 1.6 \pm 0.2$ s. Thus, for our bulk sample, other contributions to deuteron relaxation, such as librational motion, interfere with observation of Korringa-like behavior. A more complete discussion of deuteron T_{1Z} and T_{1Q} relaxation times in our Pani samples will be presented elsewhere. We believe the shifted peak represents metallic regions of the emeraldine salt, where electronic charge is delocalized. The fact that at room temperature approximately 20% of ES is crystalline, while 57% of the deuterons experience a

Table 1. Best Fit Parameters for Temperature-Dependent ^{2}H MAS Spectra of Emeraldine Salt[a]

T, K	I_1[b]	Δ_1[d], Hz	Δ_3, Hz	δ_3[e] $- \delta_1$, Hz	Δ_2, Hz
223	0.45 ± 0.02[c]	228 ± 12	981 ± 90	236 ± 79	2465 ± 2009
263	0.41 ± 0.02	240 ± 11	950 ± 47	246 ± 43	2915 ± 1657
333	0.29 ± 0.06	407 ± 56	1077 ± 120	303 ± 83	2245 ± 1573
373	0.24 ± 0.03	371 ± 39	1051 ± 220	277 ± 33	4000 ± 3350

[a] The fitting function is a normalized, weighted sum of three Gaussians as described in Appendix A. [b] I_j is the normalized integrated intensity of the jth Gaussian. The intensity of the unshifted wide peak (I_2) was fixed at 25% of I_1. See Appendix A for explanations. [c] Uncertainty limits are the observed range of values measured independently from fits of three pairs of sidebands. [d] Δ_j is the full width at half-height of Gaussian peak j. [e] δ_j is the shift from zero. The shift of a peak from zero frequency was calculated as an average of center frequencies of symmetric peaks on opposite site sides of the spectrum.

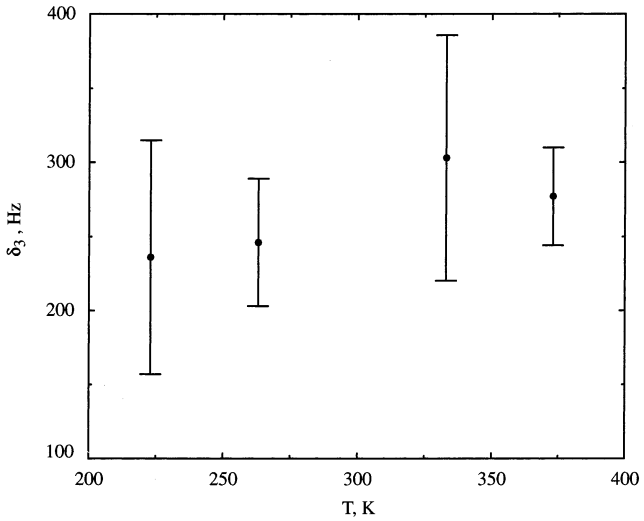

Figure 7. Temperature dependence of the shift of the "third" peak from zero frequency for emeraldine salt. It was calculated as an average of center frequencies of symmetric sidebands on opposite sides of the spectrum: $(\delta_{3n} - \delta_{3n'})/2$, where n is the sideband number.

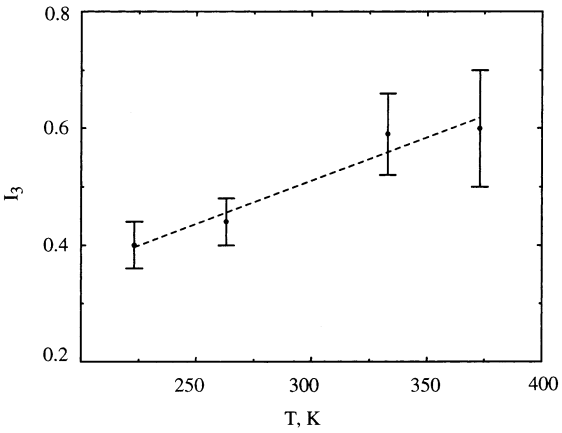

Figure 8. Temperature dependence of the integrated intensity of the shifted peak of spinning sidebands of emeraldine salt. (Dashed line is drawn to guide the eye.)

Knight shift, confirms previous conclusions[18] that electric charge is delocalized over several metallic islands.[18] Observation of the Knight shift suggests that polarons transport charge in the metallic regions. This interpretation is consistent with relatively low bulk conductivity, which is presumably limited by charge transport between spatially separated metallic regions.

As anticipated, both the conductivity[18] and the relative integrated intensity of the Knight shifted peak (see Figure 8) increase with temperature. (These intensities are not corrected for T_2; the calculations described in Appendix B show that the correction (5%) would be inconsequential.) The combination of covalent bonding along polymer chains and weak intermolecular bonding between them implies a quasi-one-dimensional system. This has an important consequence for charge delocalization: the increased intensity of the Knight-shifted peak with temperature can be attributed to an increase in the charge delocalization length. As temperature increases, quasi-1D polymer chains in disordered regions can become more aligned, thereby contributing to charge delocalization. Consequently, more deuteron spins are coupled with charge carriers, producing a more intense Knight-shifted peak.

The width at the half-maximum of the shifted peak is approximately 20 ppm and independent of temperature. It is likely that this arises from a heterogeneous charge density distribution.[26]

The two unshifted peaks of ES are very similar to those of nonconductive EB, except the broad, unshifted Gaussian is wider (at 263 K the line width of the base is $\Delta_2 = 997 \pm 190$ Hz and that of the salt is $\Delta_2 = 2915 \pm 1657$ Hz). This fact can be attributed to the existence of localized bipolarons (see Figure 1C) in emeraldine salt. For the base, the narrow peak is assigned to benzoid rings. The second (broad) Gaussian peak, relative integrated intensity of which is 25% of the narrow peak, can be attributed to doubly protonated diimine groups (bipolarons) with Cl^- counterions positioned interstitially for charge neutrality. The possibility of several overlapping wide Gaussians here, representing localized polarons and/or unprotonated regions, cannot be excluded.

The observation of the Knight shift in ES provides independent evidence to support the proposal of Ginder et al.,[27] that the insulator-to-metal transition and concomitant increase in conductivity could be due to formation of a polaron lattice. Even though the transition of a bipolaron to two polarons is not energetically favorable for many other conductive polymers,[28] formation of an ordered array of polarons, centered on alternate nitrogen atoms of polyaniline, can be stabilized by the energy gained trough delocalization and Coulomb interaction. As temperature increases, the spinless bipolarons may dissociate to form polarons, and local polarons may become part of a polaron band.

c. Pani/Clay. A typical MAS spectrum of Pani/Clay is shown in Figure 9. The best model function for simulating this spectrum was found to be a weighted sum of two Gaussians (dashed line in the inset of Figure 9; for details see Appendix A). The best fit parameters are listed as functions of temperature in Table 2. Because of the low concentration of deuterated polymer in the clay, quantitative analysis of the Pani/clay MAS spectra was complicated by very low signal-to-noise ratio. The width of the narrow peak increases with temperature from $\Delta_1 = 559 \pm 83$ Hz at 223 K to $\Delta_1 = 714 \pm 70$ Hz at 373 K. The width of the wide peak exhibits at most a very weak temperature dependence

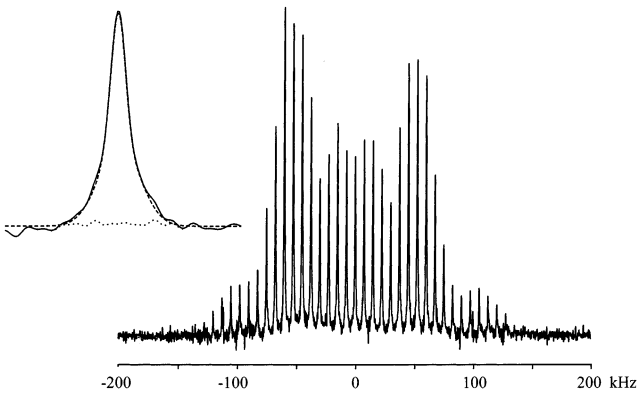

Figure 9. Experimental deuteron MAS (7.5 kHz) spectrum of Pani/MMT clay nanocomposite at 263 K. The inset illustrates a spinning sideband. The dashed line is the best fit, achieved by nonlinear Levenburg−Marquardt iterations on a normalized, weighted sum of two Gaussian functions. The dotted line is the difference between the experimental and calculated data.

(see Table 2). Fast relaxation in the sample can account for the temperature dependence of the line width. The center frequencies of both peaks are the same and are temperature-independent. One might expect to observe a third, shifted peak for ES intercalated into MMT. Unfortunately, poor signal-to-noise ratio and pronounced broadening of the sidebands obscured the spectral analysis. If present, the extra set of shifted spinning sidebands would be difficult to observe due to high intensity of the broad unshifted Gaussian (see Table 3). Qualitatively, the Pani/clay sidebands are similar to those of nonconductive EB, even though the conditions of synthesis were optimized for formation of conductive emeraldine salt. The lack of an observable Knight shift in Pani/clay is possibly a consequence of quasi-2D confinement of the polymer, which prevents formation of three-dimensional metallic islands.[18]

IV. Conclusions

In polyaniline, deuteron MAS spectra provide unique information about small chemical shifts, which is obscured in QE spectra. Individual spinning sidebands of nonconductive emeraldine base can be fit by a weighed sum of two Gaussians. Conductive emeraldine salt has an additional manifold of spinning sidebands, shifted 6 ppm toward higher frequencies. These sidebands represent metallic regions of the sample, where deuteron spins interact with delocalized electron spins (Knight shift). The observation of the Knight shift suggests that polarons are involved in charge transport. Thermal activation of quasi-particles (bipolarons and localized polarons) to delocalized (band) structures can account for the observed increase in intensity of the Knight-shifted peak with temperature (from approximately 40% at 223 K to 60% at 373 K). Failure to observe a Knight shift in the Pani/clay sample is consistent with the importance of 3D mechanisms of charge transfer for bulk conductivity in polyaniline.

Acknowledgment. This work was supported by NSF Grants CHE0079136 and DMR9973933.

Appendix A. MAS Line Shape Fitting Procedure

Line shapes of the individual sidebands in MAS spectra of the Pani samples were fit to a weighted sum of test functions by minimizing χ^2, defined as

$$\chi^2 = \sum_{i=1}^{N} \frac{1}{\sigma_1^2}\{S(\nu_i) - \sum_{j=1}^{M} I_j f_j(\nu_i,\delta_j,\Delta_j)\}^2$$

Here, $S(\nu_i)$ is the measured signal intensity at frequency ν_i, and $f_j(\nu_i,\delta_j,\Delta_j)$ is the jth Gaussian (or Lorentzian) component, centered at frequency δ_j with full width at half-maximum intensity Δ_j. The experimental integrated signal intensity as well as the intensity of each component are normalized to unity,

$$\sum_{i=1}^{N} f_j(\nu_i,\delta_j,\Delta_j) = 1$$

$$\sum_{i=1}^{N} S(\nu_i) = 1$$

$$\sum_{j=1}^{M} I_j = 1$$

Thus, the relative weight of each f_j component is I_j. Fitting a sideband to a sum of three Gaussian functions, for example, requires that eight parameters be specified: three center frequencies, three line widths, and two relative intensities. The experimental uncertainty associated with $S(\nu_i)$ is σ_i. In what follows, it is assumed that every point in the spectrum has the same absolute uncertainty, which was estimated from the noise level. With these definitions, the minimum value of χ^2 for an "acceptable" model should be on the order of N, the number of data points. Much larger values of χ^2 can be used to reject potential models, while smaller ones indicate an improper estimate of the experimental uncertainties.[29]

For EB and the Pani/clay nanocomposite, fits to model functions consisting of a single Gaussian or Lorentzian function were compared with unconstrained, five-parameter fits to a sum of two Gaussians. A typical visual comparison of fits to the different model functions for EB at 263 K is shown in Figure 10. The values of χ^2 summarized in Table 3 show that two component fits are required for both samples, and relevant best fit parameters are listed in the text. Error limits could be obtained as a byproduct of the Levenburg−Marquardt procedure used to minimize χ^2, but the more realistic error limits listed in Tables 1 and 2 were obtained instead from the range of parameter values returned by independent fits to several sidebands in each spectrum.

For ES, a weighted sum of three Gaussians was required. However, the data are not of sufficient quality to permit an unconstrained fit to the eight parameters required for this model. Since the two Gaussians needed to fit EB were found to have the same center frequency, this constraint was applied to the first two Gaussians for ES. In addition, the fitting algorithm converged reliably only when an additional parameter was fixed, $I_2 = 0.25I_1$. This resulted in only six adjustable parameters: the intensity I_1 of a Gaussian function centered at frequency δ_1 with width Δ_1, a second Gaussian at frequency $\delta_1 = \delta_2$ and width Δ_2, and a third Gaussian at frequency δ_3 with width Δ_3. It is important to note that δ_1 frequency of the first Gaussian was found to be the same within ±10 Hz as observed for EB. Table

Table 2. Best Fit Parameters for Temperature-Dependent ^{2}H MAS Spectra of Pani/Clay[a]

T, K	I_1[b]	I_2[b]	Δ_1[d], Hz	Δ_2, Hz	δ_1[e], Hz	δ_2[e], Hz
223	0.36 ± 0.04[c]	0.64 ± 0.04[c]	559 ± 83	1960 ± 559	27 ± 5	15 ± 18
263	0.39 ± 0.07	0.61 ± 0.07	555 ± 58	1831 ± 437	15 ± 10	50 ± 22
333	0.42 ± 0.06	0.58 ± 0.06	626 ± 79	2089 ± 457	18 ± 9	20 ± 24
373	0.44 ± 0.06	0.56 ± 0.06	714 ± 70	2124 ± 468	22 ± 10	19 ± 15

[a] The fitting function is a normalized, weighted sum of two Gaussians as described in Appendix A. [b] I_j is the normalized integrated intensity of the jth Gaussian. [c] Uncertainty limits are the observed range of values measured independently from fits of three pairs of sidebands. [d] Δ_j is the full width at half-height of Gaussian peak j. [e] δ_j is the shift from zero. The shift of a peak from zero frequency was calculated as an average of center frequencies of symmetric peaks on the opposite sides of the spectrum.

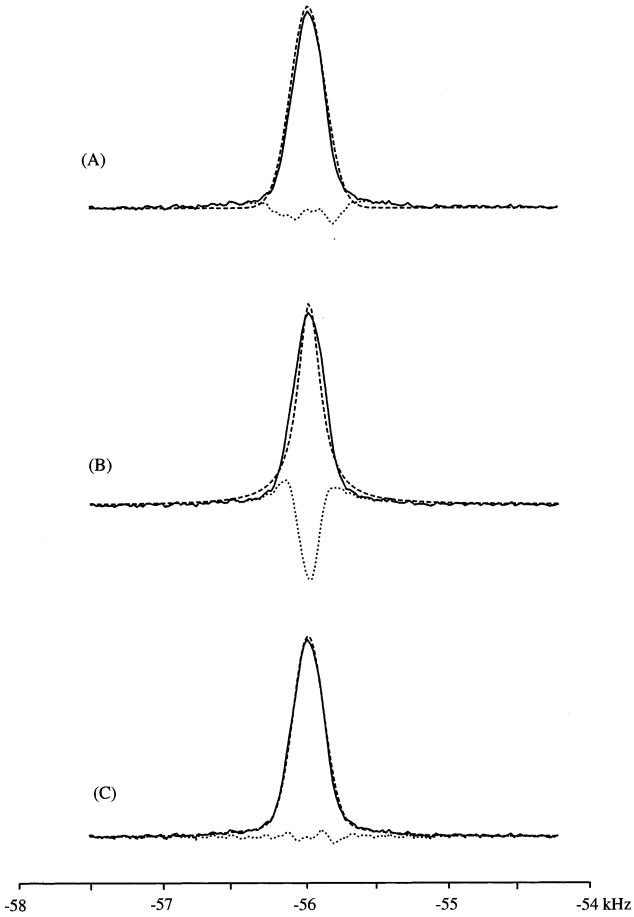

Figure 10. Comparison of experimental spectrum (solid line) of a spinning sideband of EB at 263 K with different fit functions (dashed lines): Gaussian (A), Lorentzian (B), weighted sum of two Gaussians (C). The difference between experimental and calculated line shapes is represented by dotted lines.

Table 3. Chi-Square Comparison of Different Model Functions for Emeraldine Base, Emeraldine Salt, and Pani/MMT Clay Nanocomposite at 223 K[a]

	model functions			
material	one Gaussian	two Gaussians	three Gaussians	Lorentzian
EB	12896	598		12555
ES	18695	352	231	3110
Pani/clay	2965	299		734

[a] In all cases, the number of points used in the fit was 151.

1 in the main text summarizes all the parameters determined for ES.

Appendix B. T_2 Correction for Emeraldine Salt

The time origin of the MAS spectra is the top of the first rotational echo, and relative intensities determined by deconvolution of MAS sidebands are therefore affected by differential transverse relaxation during the first rotor period. As noted in the text, this is not a problem for emeraldine base, because the echo decay was well represented by one exponential (no differential relaxation). However, semilog plots of sideband intensity vs echo number for the emeraldine salt sample (not shown) revealed significant curvature. In principle, each of the Gaussian components needed to fit the ES line shape can decay at a different rate (or even a distribution of rates). However, since a single exponential sufficed to describe relaxation of both Gaussian components for EB, we assume here that only one more exponential is needed for ES.

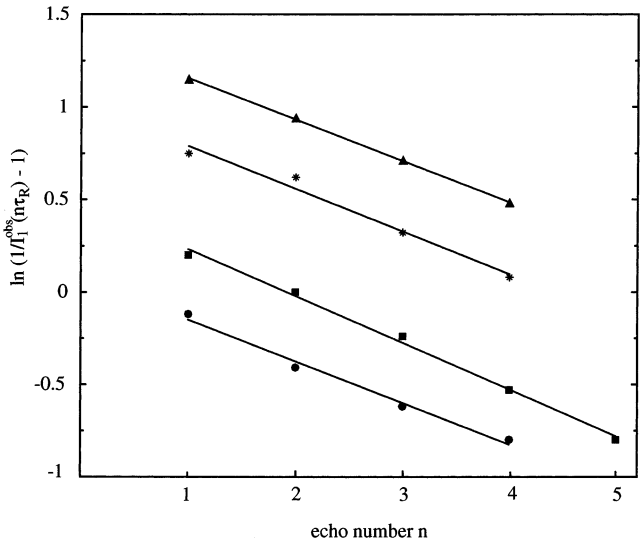

Figure 11. T_2 correction plot for emeraldine salt for different temperatures: 223 K (circles), 263 K (squares), 333 K (stars), 373 K (triangles). Solid lines are linear least-squares fits with parameters (intercept, slope) = (0.08 ± 0.05, 1.80 ± 0.48) at 223 K; (0.485 ± 0.033, 2.02 ± 0.08) at 263 K; (1.20 ± 0.07, 1.85 ± 0.19) at 333 K; (1.38 ± 0.09, 1.79 ± 0.03) at 373 K. Rotor period $\tau_R = 125$ μs.

First, a set of "T_2-relaxed" spectra was obtained by simple left shifts to the top of successive echoes. For each such spectrum, the line shape of a representative sideband was fit by unconstrained nonlinear least squares to a sum of two Gaussian components. The fractional intensities of first and second Gaussians determined by fitting are denoted by $I_1^{obs}(n\tau_R)$ and $I_2^{obs}(n\tau_R) = 1 - I_1^{obs}(n\tau_R)$, respectively, where $n = 1, 2, 3, \ldots$ is the echo number. Normalization gives

$$I_1(0)e^{-n\tau_R/T_2^{(1)}} + (1 - I_1(0))e^{-n\tau_R/T_2^{(2)}} = 1$$

Here, $T_2^{(1)}$ and $T_2^{(2)}$ are the phenomenological transverse relaxation times of the first and second components, respectively, and $I_1(0)$ is the true (integrated) intensity of the first Gaussian at $t = 0$. We note in passing that T_2 defined in this fashion bears no simple relation to

sideband line widths. The observed intensity of the first Gaussian component is then given by

$$I_1^{\text{obs}}(n\tau_R) = \frac{I_1(0)e^{-n\tau_R/T_2^{(1)}}}{I_1(0)e^{-n\tau_R/T_2^{(1)}} + (1 - I_1(0))e^{-n\tau_R/T_2^{(2)}}}$$

and hence

$$\left(\frac{1}{I_1^{\text{obs}}(n\tau_R)} - 1\right) = \left(\frac{1}{I_1(0)} - 1\right)e^{-n\tau_R(1/T_2^{(2)} - 1/T_2^{(1)})}$$

Thus, the intercept of a plot of $\ln(1/I_1^{\text{obs}}(n\tau_R) - 1)$ vs echo number n yields the corrected intensity, while the slope gives the difference in relaxation rates. Application of this procedure to data for ES is illustrated in Figure 11, with fit parameters listed in the figure caption.

The linearity of the plots at each temperature justifies the analysis in terms of just two exponentials. The relaxation time of the first Gaussian component, $T_2^{(1)}$, is on the order of 1 ms, and that of the second component, $T_2^{(2)}$, is about 0.5 ms. It follows that the correction to fractional intensities arising from differential relaxation during the first 125 μs rotor period is no more than about 5% and can be safely ignored.

References and Notes

(1) Roth, S.; Graupner, W. *Synth. Met.* **1993**, *55*−*57*, 3623−3631.

(2) Kumar, D.; Sharma, R. C. *Eur. Polym. J.* **1998**, *34*, 1053−1060.

(3) MacDiarmid, A. G.; Epstein, A. J. *Mater. Res. Soc. Symp. Proc.* **1994**, *328*, 133−144.

(4) Wessling, B. *Synth. Met.* **1998**, *93*, 143−154.

(5) Shim, Y.-B.; Stilwell, D. E.; Park, S.-M. *Electroanalysis* **1991**, *3*, 31−36.

(6) MacDiarmid, A. G. *Synth. Met.* **1997**, *84*, 27−34.

(7) MacDiarmid, A. G., Epstein, A. J. S. A., Jenekhe, K. J. W., Eds.; American Chemical Society: Washington, DC, 1997; Vol. 672, pp 395−407.

(8) Kaneto, K.; Kaneto, M.; Min, Y.; MacDiarmid, A. G. *Synth. Met.* **1995**, *71*, 2211−2212.

(9) Ray, A.; Asturias, G. E.; Kershner, D. L.; Richter, A. F.; MacDiarmid, A. G. *Synth. Met.* **1989**, *29*, E141−E150.

(10) Koziel, K.; Lapkowski, M.; Lefrant, S. *Synth. Met.* **1995**, *69*, 137−138.

(11) Kohlman, R. S.; Zibold, A.; Tanner, D. B.; Ihas, G. G.; Ishiguro, T.; Min, Y. G.; MacDiarmid, A. G.; Epstein, A. J. *Phys. Rev. Lett.* **1997**, *78*, 3915−3918.

(12) Weaver, C. E.; Pollard, L. D. *The Chemistry of Clay Minerals*; Elsevier Scientific Publishing Co.: Amsterdam, 1973; Vol. 15.

(13) Kaplan, S.; Conwell, E. M.; Richter, A. F.; MacDiarmid, A. G. *Macromolecules* **1989**, *22*, 1669−1675.

(14) Kolbert, A. C.; Caldarelli, S.; Thier, K. F.; Sariciftci, N. S.; Cao, Y.; Heeger, A. J. *Phys. Rev. B* **1995**, *51*, 1541−1545.

(15) Richter, A. F.; Ray, A.; Ramanathan, K. V.; Manohar, S. K.; Furst, G. T.; Opella, S. J.; MacDiarmid, A. G.; Epstein, A. J. *Synth. Met.* **1989**, *29*, E243−E249.

(16) Beau, B.; Travers, J. P.; Banka, E. *Synth. Met.* **1999**, *101*, 772−775.

(17) Wu, Q.; Xue, Z.; Qi, Z.; Wang, F. *Polymer* **2000**, *41*, 2029−2032.

(18) Joo, J.; Long, S. M.; Pouget, J. P.; Oh, E. J.; MacDiarmid, A. G.; Epstein, A. J. *Phys. Rev. B* **1998**, *57*, 9567−9580.

(19) Wittebort, R. J. *J. Magn. Reson.* **1989**, *83*, 626−629.

(20) Vold, R. L.; Hoatson, G. L.; Tse, T. Y. *Chem. Phys. Lett.* **1996**, *263*, 271.

(21) Spiess, H. W. *Colloid Polym. Sci.* **1983**, *261*, 193−209.

(22) Cholli, A. L.; Dumais, J. J.; Engel, A. K.; Jelinski, L. W. *Macromolecules* **1984**, *17*, 2399−2404.

(23) Hoatson, G. L.; Vold, R. L. *NMR: Basic Princ. Prog.* **1994**, *32*, 1−61.

(24) Usha, M. G.; Peticolas, W. L.; Wittebort, W. J. *Biochemistry* **1991**, *30*, 3955−3962.

(25) Mehring, M.; Rachdi, F.; Zimmer, G. *Philos. Mag. B* **1994**, *70*, 787−794.

(26) Kaplan, S.; Conwell, E. M.; Richter, A. F.; MacDiarmid, A. G. *J. Am. Chem. Soc.* **1988**, *110*, 7647−7651.

(27) Ginder, J. M.; Richter, A. F.; MacDiarmid, A. G.; Epstein, A. J. *Solid State Commun.* **1987**, *63*, 97−101.

(28) Bredas, J. L.; Street, G. B. *Acc. Chem. Res.* **1985**, *18*, 309−315.

(29) Press, W. H.; Teukolsky, S. A.; Vetterling, W. T.; Flannery, B. P. *Numerical Recipes in C*, 2nd ed.; Cambridge University Press: New York, 1992.

MA021563T